batteries

Article

Real Electric Vehicle Lithium-Ion Battery Capacity Estimation Method Based on the Fusion Model of Discrete Arrhenius and Double Extended Kalman Filter

Dongdong Qiao [1], Zhicheng Zhu [2], Xiaowei Shen [1], Zhiwei Zhao [3], Xiangjun Li [4] and Xin Lai [1,*]

[1] School of Mechanical Engineering, University of Shanghai for Science and Technology, Shanghai 200093, China
[2] School of Automotive Engineering, Jiangxi Polytechnic University, Jiujiang 332007, China
[3] The China Automotive Engineering Research Institute Co., Ltd., Chongqing 401122, China
[4] The China Electric Power Research Institute, Beijing 100192, China
* Correspondence: laixin@usst.edu.cn

Abstract

Accurate capacity estimation of lithium-ion batteries (LIBs) in real-world electric vehicles (EVs) remains a critical challenge due to complex degradation mechanisms, sparse cloud-platform data, and the limitations of existing single-model approaches. To address these issues, this paper proposes a novel fusion estimation method that integrates a discretized Arrhenius empirical lifetime model with a first-order equivalent circuit model (ECM) identified via particle swarm optimization (PSO) and employs a dual extended Kalman filter (DEKF) to synergistically update model parameters and fuse capacity estimates. Then, the proposed method is validated using real-world charging data from 36 EVs across three vehicle brands. Experimental results demonstrate that the fusion model achieves capacity estimation errors within 2.974% maximum and delivers state-of-health (SOH) estimation with R^2 values of 0.966, 0.983, and 0.981 for the three vehicle types, respectively. The method effectively overcomes data sparsity and noise issues inherent in cloud-platform data, and provides accurate, adaptive, and robust capacity tracking under diverse real-world operating conditions. This work offers a practical and scalable solution for cloud-based battery health management in next-generation EV applications.

Keywords: electric vehicle; lithium-ion batteries; capacity estimation; Arrhenius; equivalent circuit model

Academic Editors: Roberto Bubbico

Received: 23 August 2026
Revised: 15 October 2026
Accepted: 22 October 2026
Published: 2 November 2026

Copyright: © 2026 by the authors. Submitted for possible open access publication under the terms and conditions of the Creative Commons Attribution (CC BY) license.

1. Introduction

With the intensification of the global energy crisis and environmental issues, countries are seeking sustainable energy development paths, and the development and application of new energy has become a global consensus [1,2]. Under the guidance of energy structure transformation policies, the electric vehicles (EVs) industry is showing a rapid development trend, leading the global automotive industry to transform towards green and low-carbon direction [3,4]. Lithium-ion batteries (LIBs), as the core energy device of EVs, have significant importance for new energy vehicles and even the entire new energy industry [5].

In the daily charging and discharging process of LIBs, various stress conditions such as high/low ambient temperatures [6,7], high-rate charging [8,9], and calendar aging [10,11] can cause capacity degradation in various modes, such as active material particle

rupture [12,13], low-temperature lithium deposition [14,15], high-temperature gas production [16], solid electrolyte interphase (SEI) thickening [17], and active material reduction [18]. Accurately estimating capacity can help battery management system (BMS) to reduce overcharging and discharging risks, optimize thermal management strategies, and thus delay battery aging [19]. It is necessary to estimate the capacity state of the battery in the service process. However, as LIBs are complex nonlinear systems, the capacity degradation process involves complex side reaction processes that are difficult to describe using fixed mathematical and physical expressions. Moreover, the fluctuations in environment and operating conditions during the service of batteries also pose significant challenges to capacity estimation [20]. Therefore, estimating the capacity of LIBs is of great significance and full of challenges for EVs. The current research status of capacity estimation methods for batteries has been comprehensively reviewed [21,22], and the main estimation methods can be divided into three categories: analysis-based methods, model-based methods, and data-driven methods.

For the analysis-based methods, there are incremental capacity (IC) analysis method, differential voltage (DV) analysis method, differential thermal (DT) analysis method, and electrochemical impedance spectroscopy (EIS) analysis method. Shang et al. [23] obtained the optimized charging interval based on the peak distribution of the IC curves, and the battery capacity was estimated by utilizing the charging quantity of electricity within the interval. Sun et al. [24] used battery internal resistance compensation IC curve offset to achieve estimation of battery capacity with the charging time. Li et al. [25] used four aging datasets from NASA public dataset to extract IC curve features related to battery capacity, trained a Gaussian process regression (GPR) model, and evaluated the uncertainty of the model using covariance functions. Mao et al. [26] obtained strong correlation features of battery capacity based on battery DV curve, and used regression model to estimate battery capacity. Wu et al. [27] used the collected surface temperature signals of the battery and calculated the DT signal to track the phase transition in the electrode and the resulting entropy heat to evaluate the degradation of battery capacity. Due to its interpretability, fast responsiveness, and non-invasiveness, EIS is also widely used in the field of battery capacity estimation. For example, Jiang et al. [28] extracted broadband EIS, model parameters, and fixed frequency impedance three representative features from EIS as the capacity estimation features to estimate the battery capacity. Meng et al. [29] extracted physical parameters as features for estimating the aging state of batteries by fitting the equivalent circuit model with EIS measurements. However, these methods still face challenges such as random operating conditions, sampling frequency, and difficulty in online measurement of EIS, making it difficult to deploy and apply them in real-world EV environments.

For the model-based methods, it can be specifically divided into empirical models, equivalent circuit models (ECMs), and electrochemical mechanism models. Such as, Wu et al. [30] proposed a recursive total least squares estimation of battery capacity based on forgetting factors, and used the Arrhenius empirical model to correct the temperature and state of health (SOH) estimation results. ECMs simplifies the internal chemical behavior of the battery into a circuit network to describe the voltage response, internal resistance changes, and dynamic characteristics of the battery. It is often used to identify the capacity of batteries due to the inclusion of battery capacity parameters. Liu et al. [31] used recursive least squares and adaptive extended Kalman filtering algorithms to achieve joint estimation of battery state of charge (SOC) and capacity. Li et al. [32] derived a reduced order electrochemical model by analyzing the electrochemical kinetics relationship, and achieved joint estimation of battery SOC and SOH by extracting capacity related physical feature subspaces. Gao et al. [33] used Pade to approximate and simplify the pseudo two-dimensional (P2D) model, the fusion of the reduced order electrochemical model and the dual nonlinear filter was used to jointly estimate the battery SOC and capacity. Although

the above model achieves short-term capacity estimation based on fixed laboratory conditions, the battery still faces the problem of updating model parameters during service.

For the data-driven methods, it has also been widely studied due to the lack of reliance on complex mechanistic models. Dai et al. [34,35] combined reduced dimensional EIS features with six machine learning models to achieve capacity estimation under unknown SOC. Meng et al. [36] fitted the ECM with EIS measurements, extracted physical parameters as battery aging characteristics, and established a spatiotemporal long short-term memory (LSTM) network model to extract time series features for battery capacity estimation, which was validated on a public dataset. Zhao et al. [37] introduced seven layered voltage intervals from the discharge curve to extract three characteristic parameters of batteries, and used a bidirectional gate-controlled cycle unit to estimate battery capacity. Hu et al. [38] innovatively combined ampere hour integration, open circuit voltage, and resistance correction methods to label battery capacity, screened features related to battery capacity based on Pearson correlation coefficient, and used attention mechanism to enhance learning of convolutional neural network and bidirectional gated recursive unit to estimate battery capacity. These methods can achieve estimation of battery capacity, but they all rely on a large amount of experimental data for training. It is worth exploring how to ensure the quantity and quality of experimental data.

In the existing literature, although extensive research has been conducted on battery capacity estimation algorithms and different types of capacity estimation methods have been proposed, these methods are mostly based on static laboratory data and public dataset for capacity estimation algorithm validation. In the real-world EV environments, the massive high-frequency sampling data of batteries in the entire lifecycle is difficult to store in the vehicle BMS, which will be diluted from 1~10 Hz high-frequency data to 0.1~0.025Hz and transmitted to the big data cloud platform [39]. It makes traditional capacity estimation methods that rely on high-density laboratory or vehicle data unable to adapt in the cloud. Therefore, it is necessary to explore a new capacity estimation method based on sparse data on cloud platforms.

Considering the existing research gaps, a discretized Arrhenius empirical model for the lifespan of LIBs in real-world vehicles is proposed. Then, the capacity is identified based on particle swarm optimization (PSO) algorithm combined with first-order ECM. Capacity is fusion estimated to improve the accuracy and robustness using the dual extended Kalman filter (DEKF). The capacity fusion estimation method is optimized by adjusting parameter updates and weights. The main innovations are summarized as follows:

1) Discrete three-parameter Arrhenius model for iterative capacity prediction using sparse cloud data.
2) DEKF framework for synergistic fusion of empirical model and PSO-ECM identification results.
3) Tunable coefficient in extended Kalman filter (EKF) to adaptively adjust ECM correction strength on model parameters.

The remainder of this study is organized as follows. Section 2 provides a detailed introduction to the capacity estimation method for real-world EV's battery data on big data cloud platforms. The cloud data used to validate the proposed capacity estimation method are presented in Section 3. Section 4 validates the capacity estimation results of the proposed fusion model and discusses them. Finally, Section 5 concludes the fusion capacity estimation method proposed in this study.

2. Methodology

2.1. Capacity Identification

Accurate estimation of SOH is crucial for ensuring the safety, reliability, and service life of lithium-ion batteries. However, the actual operating conditions of batteries are extremely complex, and direct measurement of battery capacity poses significant challenges. To address this issue, this chapter proposes a battery capacity identification method based on the combination of PSO and ECM. This method introduces battery capacity as one of the parameters to be identified into the ECM and utilizes the PSO algorithm to optimize the model parameters, thereby achieving accurate estimation of battery capacity.

Among various ECMs, the 1-RC model is the most commonly used type, as shown in Figure 1, as it offers a good balance between computational efficiency and accuracy. Therefore, this study chooses the 1-RC ECM for battery capacity identification, with the principle illustrated in Equation (1)

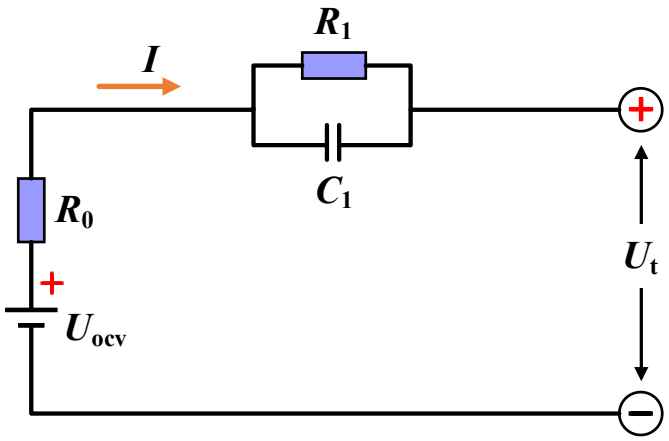


Figure 1. 1-RC model.

$$U_t = U_0 + U_1 + U_{ocv} = IR_0 + U_1 + U_{ocv} \tag{1}$$

where U_{ocv} represents the battery OCV, U_0 denotes the polarization voltage caused by the ohmic internal resistance R_0, U_1 signifies the polarization voltage caused by the polarization internal resistance R_1, U_t stands for the battery terminal voltage, and I indicates the current. The calculation formula for the polarization voltage U_1 is:

$$\dot{U}_1 = -\frac{1}{R_1 C_1} U_1 + \frac{1}{C_1} I \tag{2}$$

$$\tau = R_1 C_1 \tag{3}$$

where R_1 represents the polarization internal resistance, C_1 denotes the polarization capacitance, and τ signifies the time constant. Once the parameters of the ECM are known, the terminal voltage U_t of the model can be calculated using Equation (1). Considering Equation (2) as a linear time-invariant system, Equation (3) can be derived.

$$U_{1,\ k+1} = e^{-\frac{\Delta t}{\tau}} U_{1,\ k} - (1 - e^{-\frac{\Delta t}{\tau}}) R_1 I_k \tag{4}$$

where $U_{1,k+1}$ represents the polarization voltage U_1 at time $k+1$, Δt is the interval sampling time, $U_{1,k}$ represents the polarization voltage U_1 at time k, and I_k represents the current value at time k.

When utilizing an ECM for parameter identification, the ECM itself does not directly incorporate the battery capacity value. To address this issue, establishing an effective connection between capacity and ECM becomes a necessary step. Given that U_{ocv} in Equation (1) represents the OCV of the battery, and there exists a stable mapping relationship between OCV and SOC, introducing an ampere-hour integration model becomes an effective approach to establish the correlation between ECM and capacity. Its mathematical expression is shown in Formula (5)

$$SOC = SOC_0 + \frac{\int Idt}{Cap} \tag{5}$$

where SOC_0 represents the initial *SOC* value, I represents current, t represents time, and *Cap* represents battery capacity.

Since the mapping relationship between U_{ocv} and SOC is established, under the conditions of specifying current I and time t, the relationship as shown in Formula (6) can be further derived

$$U_{ocv} = f(SOC) = f(SOC_0 + \frac{\int Idt}{Cap}) \tag{6}$$

Substituting Formula (6) into Formula (1), we obtain Formula (7)

$$U_t = IR_0 + U_1 + f(SOC_0 + \frac{\int Idt}{Cap}) \tag{7}$$

The set of parameters to be identified for ECM is [SOC_0, *Cap*, R_0, R_1, τ], encompassing key parameters such as the initial *SOC* (SOC_0), battery capacity (*Cap*), ohmic internal resistance (R_0), polarization internal resistance (R_1), and time constant (τ). Based on this, the PSO algorithm can be utilized to precisely identify these parameters, thereby obtaining the optimal battery capacity value.

The parameter range for Cap is based on the nominal capacity C_0 and set to [1.2C_0, 0.7C_0]. The parameter ranges for R_0 and R_1 can be set to [0 mΩ, 1000 mΩ]. The parameter range for τ can be empirically selected as [0 s, 2800 s]. Set the root mean square error (RMSE) objective function between the terminal voltage and the reference terminal voltage, which can be described as Equation (8)

$$\mathrm{RMSE} = \sqrt{\frac{1}{n}\sum_{t=1}^{n}(U_t - U_{\mathrm{t,ECM}})^2} \tag{8}$$

where U_t represents the reference terminal voltage at time t, which is the collected value from the BMS sensor. $U_{\mathrm{t,ECM}}$ represents the model-calculated terminal voltage at time i.

In the parameter identification process, the original charging data of the vehicle are first extracted, mainly including the battery's charging voltage, charging current, and SOC data. Then, segments with a charging ΔSOC > 70% are filtered from the original data. Subsequently, the processed data are imported into the joint model algorithm based on ECM-PSO. This algorithm utilizes the optimization characteristics of PSO to adjust the parameters of ECM

during continuous iteration, ensuring that the model's calculation results closely match the actual situation. Set the population size of PSO algorithm to 300 and the number of iterations to 15 to achieve a balance between computational efficiency and identification accuracy. Finally, based on the ECM-PSO model, various parameters of ECM are successfully identified, and the key capacity identification values are also accurately obtained.

2.2. Arrhenius Model

The Arrhenius model, as an empirical model, is established with temperature as the accelerating stress and based on the main attenuation mechanism of thickening of the negative electrode SEI film [30,40]. The Arrhenius empirical decay model is an extension of the Arrhenius equation and is commonly used to describe the relationship between chemical reaction rate and temperature. In battery life prediction, the Arrhenius model is widely used to describe the variation of battery capacity over time and temperature. Its basic form is

$$\frac{dQ}{dt} = -A \cdot \exp\left(-\frac{E_a}{RT(t)}\right) \tag{9}$$

Among them, Q is the battery capacity, A is the pre-exponential factor, E_a is the activation energy, R is the gas constant, and $T(t)$ is the temperature change over time.

At a discrete time step $\Delta t_k = t_{k+1} - t_k$, integrate the above equation:

$$Q_{k+1} - Q_k = -A\int_{t_k}^{t_{k+1}} \exp\left(-\frac{E_a}{RT(\tau)}\right) d\tau \tag{10}$$

where temperature T is considered a constant and denoted as T_k at each discrete time step [t_k, t_{k+1}]. The rationality of this assumption lies in: (a) Our data sampling interval is usually several seconds to tens of seconds, during which the temperature change is minimal. (b) The battery has a large thermal inertia, and the temperature will not undergo drastic changes. Under this assumption, the integral term can be simplified:

$$Q_{k+1} - Q_k = -A \bullet \exp\left(-\frac{E_a}{RT_k}\right) \bullet \Delta t_k \tag{11}$$

$$Q_{k+1} = Q_k - A \bullet \exp\left(-\frac{E_a}{RT_k}\right) \bullet \Delta t_k \tag{12}$$

Furthermore, in order to embed this relationship into the framework of extended Kalman filtering, we have rewritten it into a standard state transition form. If the state vector contains a capacity Q, then the state transition equation is:

$$Q_{k+1} = f(Q_k, T_k, \Delta t_k) \tag{13}$$

$$f(Q_k, T_k, \Delta t_k) = Q_k - A \bullet \exp\left(-\frac{E_a}{RT_k}\right) \bullet \Delta t_k \tag{14}$$

Due to the fact that the object of this study is batteries under real-world EV operating conditions, the initial capacity is set to the nominal capacity corresponding to each vehicle model. Although the Arrhenius empirical model can accurately estimate battery capacity in a short period of time, it still faces the challenge of online updating of model parameters during long-term cycling. Therefore, other capacity estimation methods are needed to update the Arrhenius model parameters.

2.3. Fusion Model Based on DEKF Model

EKF has important application value in the field of complex system state estimation. The essential feature of the EKF algorithm is the use of local linearization strategy to handle nonlinear system modeling problems [39]. The technical implementation path is to approximate the nonlinear state equation and observation equation through first-order Taylor expansion, obtain the corresponding Jacobian matrix to replace the system matrix in the original Kalman filter (KF), and thus construct a state estimation framework suitable for nonlinear scenarios. It has been widely applied in fields such as BMS, target tracking, and robot localization [41,42].

EKF consists of two main steps: prediction and update. The update steps are shown in Table 1. Through the above steps, EKF can recursively estimate the system state and gradually reduce the estimation error.

Table 1. EKF prediction and update steps.

Steps	Equation	Description
Prediction steps		
1. State prediction	$x_{k\|\|k-1} = f(x_{k-1\|\|k-1}, u_k)$	$x_{k\|\|k-1}$ is the predicted value of the state at time k
2. Covariance prediction	$P_{k\|\|k-1} = F_k P_{k-1\|\|k-1} F_k^T + Q_k$	F_k is the Jacobian matrix, $P_{k\|\|k-1}$ is the covariance matrix for prediction, Q_k is the covariance matrix of process noise.
Update steps		
3. Kalman gain calculation	$K_k = P_{k\|\|k-1} H_k^T (H_k P_{k\|\|k-1} H_k^T + R_k)^{-1}$	K_k is the Kalman gain, H_k is the Jacobian matrix of the observed function h, R_k is the covariance matrix of the observed noise.
4. Status update	$x_{k\|\|k} = x_{k\|\|k-1} + K_k(z_k - h(x_{k\|\|k-1}))$	z_k is the real observation value, $x_{k\|\|k}$ is the estimated value of the state at time k.
5. Covariance update	$P_{k\|\|k} = (I - K_k H_k) P_{k\|\|k-1}$	

DEKF is a parallel executed dual filtering architecture, in which one EKF is used for state estimation and the other for parameter estimation. In this study, DEKF was used to update the parameters of the discrete Arrhenius model and fuse the capacity results for estimation, which can overcome the shortcomings of single data-driven models and empirical models, thereby achieving accurate estimation of capacity. The principle of the capacity estimation fusion model based on dual DEKF is shown in Figure 2. Firstly, input the defined initial parameters x_k into the discrete Arrhenius lifetime decay model to obtain the predicted capacity $C_A(x_k, n_{k+1})$ of the model under this cycle. Compare $C_A(x_k, n_{k+1})$ with the ECM based capacity estimation values $C_{KF}(n_{k+1})$ under the same cycle and use a separate EKF-#1 to calibrate and update the parameters. Reinput the

updated model parameters x_{k+1} into the discrete Arrhenius lifetime decay model to obtain the updated model prediction values $C_A(x_{k+1}, n_{k+1})$. Compare the new model prediction values $C_{KF}(n_{k+1})$ with the ECM-based capacity estimation values and obtain the calibrated fusion capacity value $C_F(n_{k+1})$ through EKF-#2. This fusion capacity value will serve as the starting capacity for the next cycle. Through this iterative process, the algorithm can achieve the fusion estimation of battery capacity and life prediction, effectively combining the advantages of the two methods to improve the accuracy and reliability of lithium battery capacity estimation and prediction.

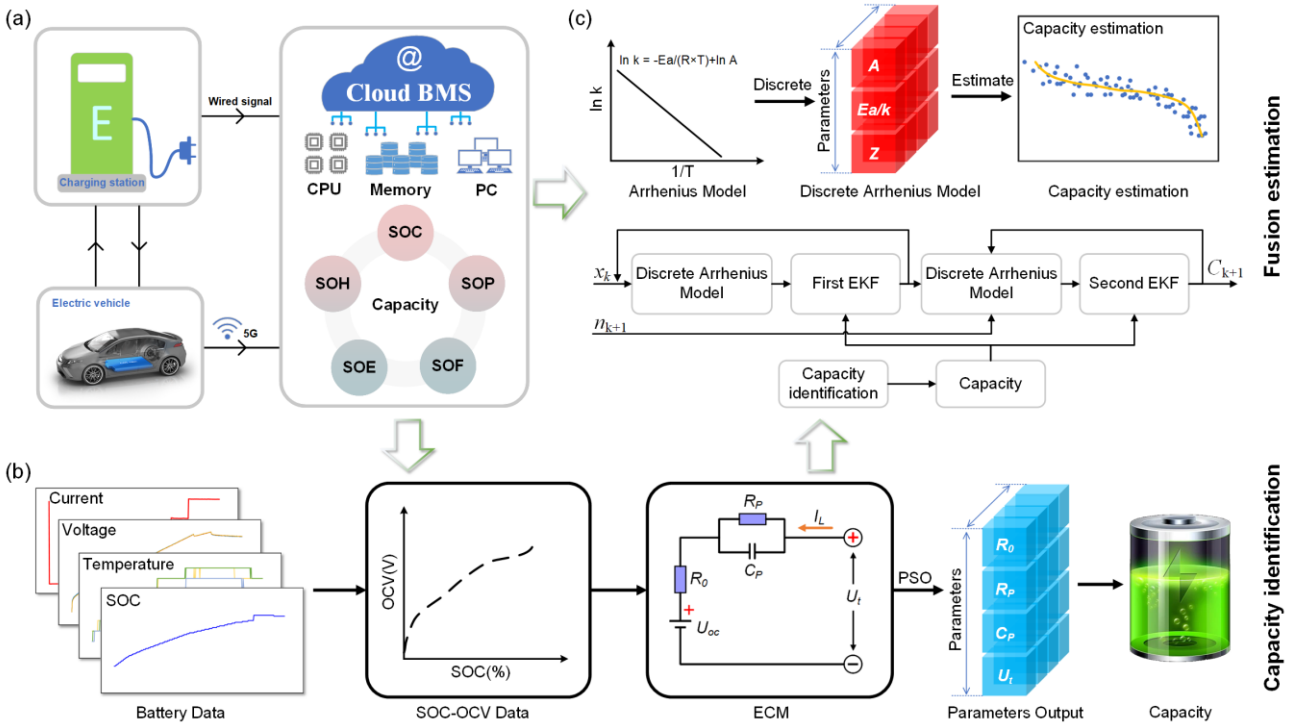


Figure 2. DEKF model fusion estimation framework. (**a**) Electric vehicle cloud BMS; (**b**) Capacity identification model based on PSO; (**c**) Capacity estimation model based on discrete Arrhenius.

2.3.1. EKF-#1 Discrete Arrhenius Model Parameter Update

In the first EKF of the DEKF used for updating the parameters of the Arrhenius model, three model parameters are first treated as state space variables, namely:

$$x_k = \begin{bmatrix} A_k \\ \left(\frac{E_a}{R}\right)_k \\ z_k \end{bmatrix} \tag{15}$$

According to the relationship between the Arrhenius capacity decay model and model parameters, the discrete space state equation and observation equation can be obtained:

$$\begin{cases} x_{k+1} = F \cdot x_k + w_k \\ y_{k+1} = g(x_k, n_{k+1}) + v_k \end{cases} \tag{16}$$

where k is the number of capacity measurements, y_{k+1} is the observation value at time k+1, namely $C_{KF}(n_{k+1})$. $g(x_k, n_{k+1})$ is the measurement function, which represents the estimation result of the Arrhenius capacity decay model under parameter x_k and cyclic n_{k-1}, namely $C_A(x_k, n_{k+1})$. ω_k is the system noise, v_k is the observation noise; their covariance is $Q_k = E\left[w_k\ w_k^T\right]$ and $S_k = E\left[v_k\ v_k^T\right]$, and F is the state transition matrix.

The process of updating the model parameter equation using EKF-#1 is shown in Table 2.

Table 2. EKF-#1 discrete Arrhenius model parameter update process.

Steps	Equation	Description
Initialization	$x_{0\|0} = \mu_0 \quad P_{0\|0} = p_0$	Initialization of model parameters and error covariance
Time update	$x_{k+1\|k} = F \cdot x_{k\|k}$, $P_{k+1\|k} = F \cdot P_{k\|k} \cdot F^T + Q_k$	$x_{k+1\|k}$ and $P_{k+1\|k}$ are the model parameters and prior estimation of error covariance at time k+1 of the system
Kalman gain	$K_{k+1} = P_{k+1\|k} \cdot \left[P_{k+1\|k} + S_{k+1}\right]^{-1}$	K_{k+1} is the Kalman gain of the system
Measurement update	$x_{k+1\|k+1} = x_{k+1\|k} + K_{k+1} \cdot \left[y_{k+1} - g(x_{k+1\|k}, n_{k+1})\right]$ $P_{k+1\|k+1} = \left[I - K_{k+1}\right] \cdot P_{k+1\|k}$	Update of model parameters and estimated error covariance values

The model parameters need to be fitted with multiple historical capacity values in order to obtain them, which means the influence of historical data needs to be considered. Here, historical errors ζ_{k+1} are introduced to calculate the average relative error between the estimated values of the *1*-th to k+1-th discrete Arrhenius model (model parameters x_k) and the capacity estimate obtained by KF filtering, as shown in Equation (19)

$$\zeta_{k+1} = \frac{\sum_{i=1}^{k+1} \frac{C_A(x_k, n_i) - C_{KF}(n_i)}{C_{KF}(n_i)}}{k+1} \tag{17}$$

Introducing ζ_{k+1} into the state transition matrix F and then updating the time in the EKF iteration equation can obtain the prior estimates of the model parameter values.

$$F = \begin{bmatrix} 1 & & \\ & 1 & \\ & & 1 \end{bmatrix} + M \cdot \zeta_{k+1} \tag{18}$$

where M is the integration matrix used to adjust parameters.

2.3.2. EKF-#2 Discrete Arrhenius Model Fusion Estimation

In the second EKF of the DEKF used for fusion capacity estimation, the updated model parameters from the Section 2.3.1 are input into the discrete Arrhenius empirical model to obtain the model prediction value at this time, which is then fused with the

estimation value based on the ECM to obtain the fusion capacity at this time. In the second EKF, based on the predicted values of the discrete Arrhenius empirical model as state space variables, the obtained discrete space state equation and state equation are:

$$\begin{cases} x'_{k+1} = g(x_{k+1}, n_{k+1}) + w'_k \\ y'_{k+1} = H \cdot x'_{k+1} + v'_k \end{cases} \tag{19}$$

where x'_{k+1} is the optimal fusion capacity of the system state at time k+1, that is $C_F(n_{k+1})$. $g(x_{k+1}, n_{k+1})$ is the conversion function, which represents the capacity estimation result of the discrete Arrhenius empirical model under parameter x_{k+1} and battery cycle n_{k+1}, i.e., $C_A(x_{k+1}, n_{k+1})$. y'_{k+1} is the observation value at time k+1, that is $C_{KF}(n_{k+1})$. H is the measurement system parameter. w'_k and v'_k represent system noise and observation noise, respectively, with covariance values of $Q'_k = E\left[w_k, {w_k}^T\right]$ and $S'_k = E\left[v_k, {v_k}^T\right]$. The process of updating the model parameter equation using EKF-#2 is shown in Table 3.

Table 3. EKF-#2 fusion estimation process.

Steps	Equation	Description
Initialization	$P'_{0\|0} = P'_0$	Error covariance initialization
Time update	$x'_{k+1} = g(x_{k+1}, n_{k+1}) + w'_k$, $P'_{k+1\|k} = P'_{k\|k} + w'_k$	$x'_{k+1\|k}$ and $P'_{k+1\|k}$ are the model parameters and prior estimation of error covariance at time k+1 of the system
Kalman gain	$K'_{k+1\|k} = P'_{k+1\|k}\left[HP'_{k+1\|k}H^T + S'_{k+1}\right]$	Kalman gain of the system
Measurement update	$x'_{k+1\|k+1} = x'_{k+1\|k} + K'_{k+1}\left[y'_{k+1} - Hx'_{k+1\|k}\right]$ $P'_{k+1\|k+1} = \left[I - K'_{k+1}\right]P'_{k+1\|k}$	Fusion capacity, error covariance estimation value update

2.4. Performance Assessment

This study evaluates the performance of the proposed fusion model using indicators such as maximum error (*Max Error*), mean absolute error (*MAE*), mean absolute percentage error (*MAPE*), normalized *RMSE*, and coefficient of determination (R^2), which are defined as follows:

$$Max\ Error = \max\left|y_i - \hat{y}_i\right| \tag{20}$$

$$MAE = \frac{1}{n}\sum_{i=1}^{n}\left|y_i - \hat{y}_i\right| \tag{21}$$

$$MAPE = \frac{1}{n}\sum_{i=1}^{n}\left|\frac{y_i - \hat{y}_i}{y_i}\right| \times 100\% \quad (22)$$

$$RMSE = \sqrt{\frac{1}{n}\sum_{i=1}^{n}(y_i - \hat{y}_i)^2} \quad (23)$$

$$R^2 = 1 - \frac{\sum_{i=1}^{n}(y_i - \hat{y}_i)^2}{\sum_{i=1}^{n}(y_i - \bar{y})^2} \quad (24)$$

where y_i and $\hat{y}_i$ are the observed and estimated SOH, respectively, and $\bar{y}$ is the mean value of observed SOH.

3. Experiment and Cloud Data Acquisition

3.1. Experiments Data of the Battery Pack

The OCV data of battery is the basic input data for battery capacity identification, in order to use ECM to achieve online estimation of battery capacity, it is necessary to test the OCV data of different vehicle batteries. This study obtained the fresh LIBs for corresponding vehicle models from three vehicle companies. The battery capacities of Vehicle-A, B, and C are 150 Ah, 177 Ah, and 216.2 Ah, respectively. Each positive electrode material of the battery is ternary lithium batteries ($LiCo_xNi_yMn_{1-x-y}O_2$, NCM), and the negative electrode is graphite. The detailed battery main parameters are shown in Table 4.

Table 4. Main parameters of three types of vehicle batteries.

Vehicle Brands	Battery Cell	Battery Shape	Capacity of Battery Cells/Ah	Charging Cut-Off Voltage/V	Discharge Cut-Off Voltage/V
Vehicle-A	Cell A	Prismatic cell	150	4.35	2.75
Vehicle-B	Cell B	Prismatic cell	177	4.25	2.5
Vehicle-C	Cell D	Cylindrical cell	216.2	4.25	2.5

Due to the fact that the equilibrium state of electrochemical reactions inside the battery changes with temperature, the battery has different OCV value at different temperature states. This study conducted hybrid pulse power characterization (HPPC) tests on the three types of batteries mentioned above at −5, 5, 15, 25, 35, and 45 °C. In order to ensure the accuracy of OCV-SOC test results, HPPC testing is performed by a Neware CE-6008-Std-6V600A battery testing bench. The voltage testing accuracy of this testing equipment is 0.1 mV, and Binder thermal chamber is used to control the battery temperature during the battery testing process. The OCV-SOC test results of different types of batteries are shown in Figure 3. It can be seen that the OCV of each battery is positively correlated with temperature, and the higher the temperature, the relatively larger the OCV. Based on these OCV data, this study can use ECM parameter identification to identify the current capacity values of each battery online.

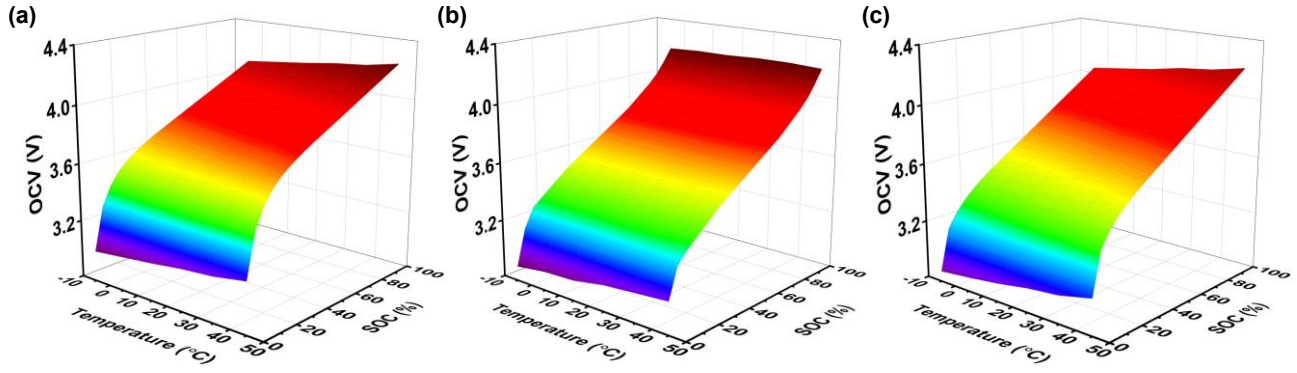


Figure 3. Real-world vehicle OCV-SOC data. (**a**) Vehicle-A; (**b**) Vehicle-B; (**c**) Vehicle-C.

3.2. Cloud Platform EV Battery Data

In order to verify the accuracy of the method proposed in this article, this study obtained usage data of 300 EVs of three brands with different operating ranges from Shanghai EV public data collecting, monitoring and research center (SHEVDC). Figure 4 shows the total driving mileages of 100 vehicles from each of the three brands. 12 vehicles from each brand were random selected for the verification of the aforementioned capacity estimation method.

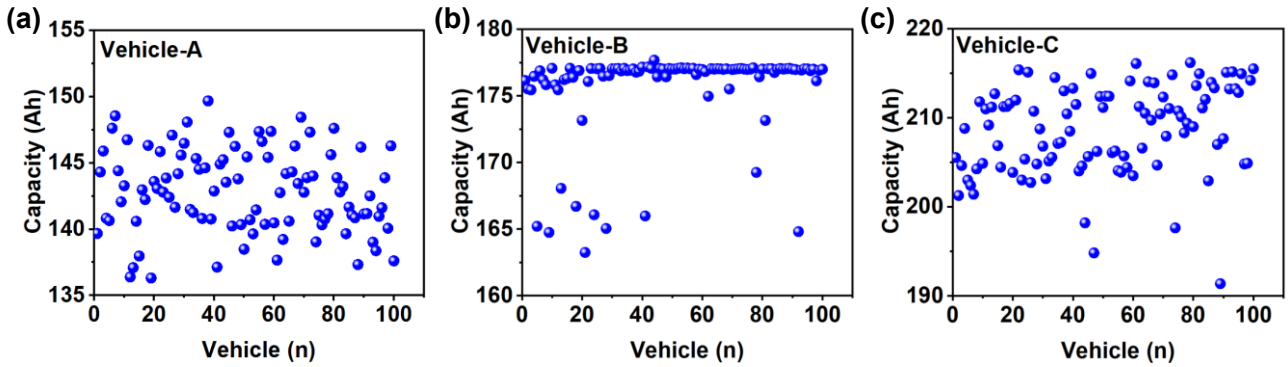


Figure 4. Capacity of 100 vehicles for brand A/B/C. (**a**) Vehicle-A; (**b**) Vehicle-B; (**c**) Vehicle-C.

The data collected under real vehicle operating conditions primarily include vehicle operation data (such as vehicle position, speed, mileage, SOC, motor status, etc.), batteries charging/discharging data (such as charging start and end time, charging power, etc.), and environmental data (such as temperature, mild road conditions, etc.). Unlike the battery testing data of professional laboratory testing equipment, these data from the cloud platform not only contain a lot of noise, but also have inconsistencies, missing, and other abnormal issues. If they are not optimized and processed, it will affect the accuracy of capacity estimation. In order to address the aforementioned data quality issues, abnormal values of charging current, voltage, SOC, and temperature that exceed the normal working range are firstly removed. Based on the recording frequency of 0.1 Hz of the battery data, linear interpolation is used to fill in the excluded abnormal values and the missing data. In addition, the synchronization of current, voltage, and SOC data can also affect the capacity calculation results of the battery. Here, we extract the current, voltage, and SOC step signals at the starting position of the charging process, using the rising edge of the step signal as the starting point for battery charging, and align the current, voltage, and SOC data.

Figures 5b–e show the charging/discharging current, SOC, 96 individual cell voltage and 48 temperature measurement signal results of one vehicle. The current, SOC, and voltage of the vehicle fluctuates greatly, and the starting and ending SOC of charging are relatively random. In addition, from the voltage subgraph of this vehicle, it can be seen

that there is a multi-stage variable current charging mode in the charging condition of the vehicle. The random SOC changes and multi-stage charging conditions in these real-world charging conditions, not only makes it impossible to obtain standard battery capacity values using ideal full and empty charging/discharging conditions but also increases the difficulty of online estimation of battery capacity.

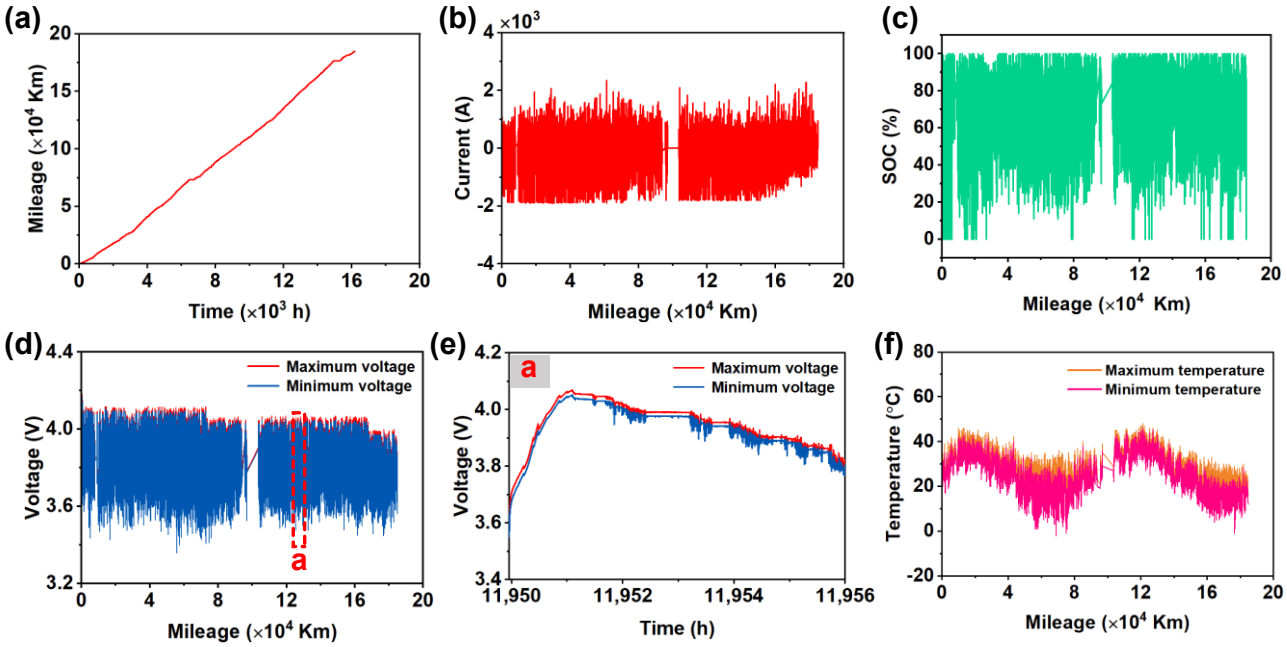


Figure 5. Real-world vehicle data. (**a**) Mileage of one vehicle; (**b**) Current; (**c**) SOC; (**d**) Voltage; (**e**) Local voltage curves; (f) Temperature.

4. Real-World Vehicle Capacity Fusion Estimation Results

4.1. Capacity Label Acquisition

Accurately obtaining battery capacity label values is an important and challenging task in the process of capacity estimation. Under standard operating conditions, the accurate capacity measurement method is to perform three complete constant current charging and discharge cycles at 25 °C and use the average of the three discharge capacities as the actual capacity of the battery. However, in a real car environment, in order to avoid stopping the vehicle due to battery depletion during driving, users usually do not empty the battery before charging, which makes obtaining accurate capacity labels in a real car environment challenging [43]. Under real vehicle operating conditions, the inverse ampere hour integration method is commonly used for capacity estimation. However, SOC estimation also often has a certain cumulative error, which is the main source of capacity estimation error in the inverse ampere hour integration method. Figures 6a,b show the normal charging voltage curves and accurate SOC estimation results of EVs. During the charging process, the battery cell voltage gradually increases, and when the maximum cell voltage reaches the cut-off voltage, its SOC also rises to 100%, this indicates that the estimated SOC value of the battery is relatively accurate. However, when there is an error in the SOC estimation of the battery (Seen Figure 5c,d), when the maximum voltage of the individual cell reaches the charging cut-off voltage, the SOC has not reached 100% SOC, and the battery is actually fully charged at this time. Therefore, the BMS will directly adjust the SOC value from 92% to 100%, which is the top correction phenomenon of the true SOC estimation of EVs. This indicates that there is an error in the initial SOC (8% SOC) of the vehicle during charging. If the uncorrected initial SOC is directly used to calculate the battery capacity, it will increase the estimation error of the battery capacity. To improve

the accuracy of battery capacity estimation, this study requires correction based on the SOC jump value at the charging end when using inverse ampere hour integration to calculate battery capacity. Taking Figure 6d as an example, the initial SOC is adjusted from 10 to 2%, while the SOC at the end of charging remains at 100%.

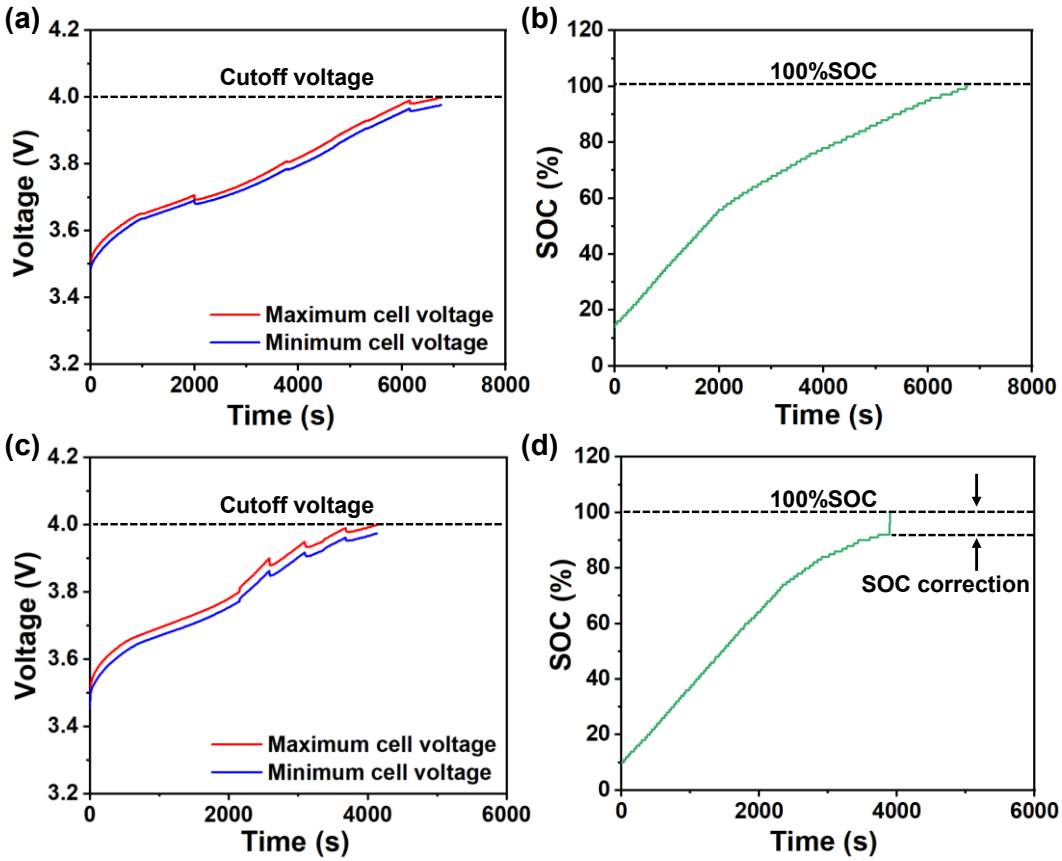


Figure 6. SOC correction during charging process. (**a**) Normal charging voltage curves; (**b**) Normal SOC curve; (**c**) SOC correction charging voltage curve; (**d**) SOC correction.

In addition, the inverse ampere hour integration method is affected by the charging SOC range when used, and it is generally believed that the larger the ΔSOC, the more accurate the calculated capacity. Due to the influence of user usage habits, different charging data have different charging ΔSOC ranges, so the accuracy of battery capacity estimation has not been improved. This study screened different charging ΔSOC ranges and selected charging data with a charging ΔSOC range greater than 70% for capacity estimation, while data with a charging ΔSOC range less than 70% will not be subjected to capacity estimation. The filtering results of charging data for a single vehicle are shown in Figure 7a. All current data have a charging ΔSOC greater than 70%. Then, these data are used to calculate the capacity values of each charging segment, as shown by the red curve in Figure 7b. However, the battery capacity calculated based on inverse ampere hour integration still has significant fluctuations and cannot accurately reflect the decay law of battery life. This study further uses KF algorithm to smooth it, and the filtered capacity is shown in the red curve in Figure 7b. The process noise covariance matrix Q and the measurement noise covariance matrix R are both 0.05, and the initial covariance matrix P_0 is 5% of the rated capacity. When tested within the range of Q values from 0.01 to 0.1, the average error change in the final capacity estimation is less than 0.5%. This indicates that the estimator is not in an extremely sharp parameter sensitive region.

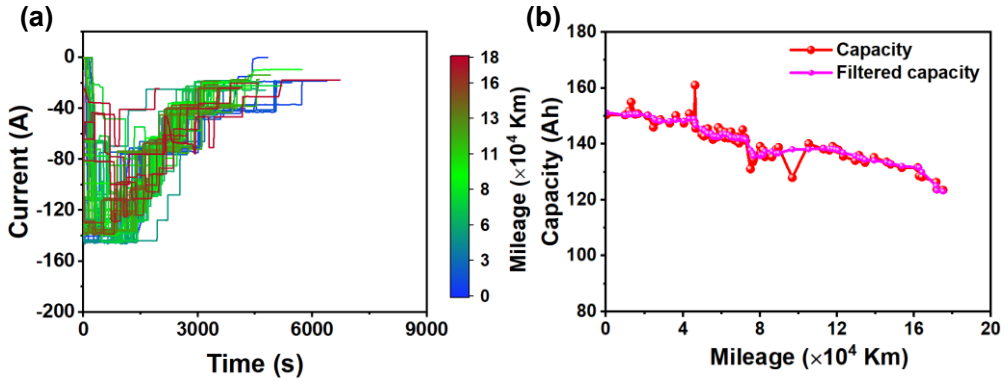


Figure 7. Capacity label of inverse ampere hour integral. (**a**) Selection of charging current; (**b**) Capacity label after filtering.

4.2. Capacity Identification Result

To verify the effectiveness of the parameter identification of the proposed equivalent circuit model, this study extracts a segment with a wide range of charging SOC from Vehicle 1 for parameter identification method validation, as shown in Figure 8. Figures 8a,b represent the charging SOC and current curves for the charging cycle, respectively. The charging SOC range is 8% to 94%, which is the corrected SOC result. In real-world vehicle environments, the battery system is usually composed of tens to hundreds of battery cells connected in series, resulting in multiple cell voltage sampling results. The system capacity is usually limited by the smallest capacity battery, and the charging voltage curve of the smallest capacity battery is usually the largest, exhibiting the maximum cell voltage (see Figure 7a). Therefore, this study chooses the maximum cell voltage for equivalent circuit model capacity identification, as shown in Figure 8c. In Figure 8c, the red curve represents the maximum voltage curve, and the blue curve represents the voltage identification result of the equivalent circuit model. The maximum voltage identification error is 20 mV.

To verify the effectiveness of the proposed capacity identification method, this study selected four different charging cycles and then utilized the ECM to identify their model parameters and capacity values. The results are presented in Table 5. From the parameter identification results in the table, it can be seen that the identification of five model parameters, namely SOC_0, R_0, R_1, τ, and Cap, can be achieved. Due to the relatively large SOC range of the four charging segment data selected in this study, with ΔSOC values of 84%, 91%, 88%, and 82% respectively. If the capacity increment method is used to estimate the capacity of the above four sets of charging data, relatively accurate capacity label values can be obtained. The capacity results calculated using the incremental capacity method are 155.31 Ah, 146.91 Ah, 144.78 Ah, and 127.32 Ah, with capacity errors of −2.30%, 1.15%, −1.82%, and 3.31%, respectively. The above results indicate that the method proposed in this study, which is based on parameter identification of equivalent circuit models, can achieve accurate estimation of battery capacity.

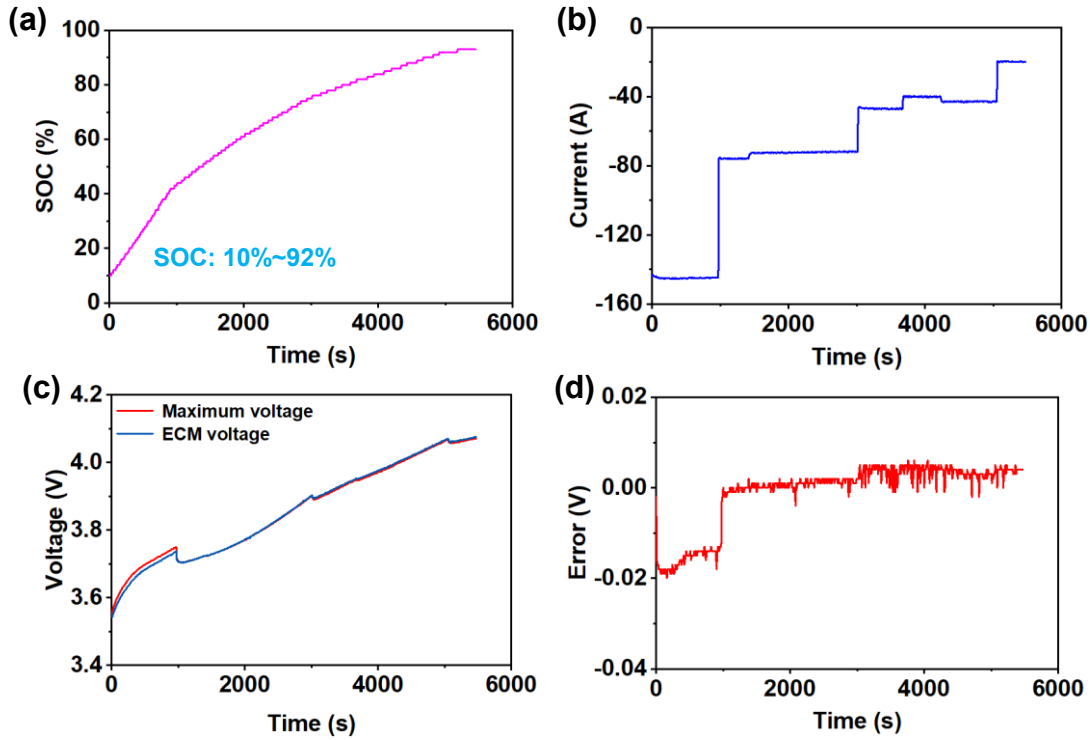


Figure 8. Voltage identification results based on ECM. (a) Charging SOC curve; (b) Charging current curve; (c) Charging voltage curve and ECM voltage output results; (d) Voltage estimation error of ECM.

Table 5. Parameter identification results.

Groups	SOC Range (%)	SOC_0 (%)	R_0 (mΩ)	R_1 (mΩ)	τ (s)	*Cap* (Ah)
1	7~91	18.19	12.53	23.26	18.22	151.74
2	9~100	12.32	14.01	30.11	26.35	148.60
3	12~100	15.63	17.82	38.60	37.83	142.14
4	10~92	10.21	19.69	51.13	55.88	131.53

4.3. Capacity Estimation Results for Different Vehicle

Figure 9 shows the capacity estimation results of some vehicles of Vehicle-A. The purple dotted line represents the capacity label values obtained through inverse ampere hour integration and KF, while the blue dotted line represents the parameter identification and Arrhenius capacity fusion estimation results. It can be seen that the batteries of all 12 vehicles show a significant decrease in capacity, and the fusion model's battery capacity estimation results have good follow-up with the inverse ampere hour integration capacity estimation results. Only in a few intervals where the capacity fluctuation is relatively large, the position error is relatively large. Among them, the capacity estimation result of Vehicle-46 is the worst, with a maximum estimation error of 2.974%, while the capacity estimation error of Vehicle-50 is the smallest, with a maximum estimation error of only 1.20%. This indicates that the fusion estimation algorithm proposed in this study has a good effect on real vehicle capacity estimation.

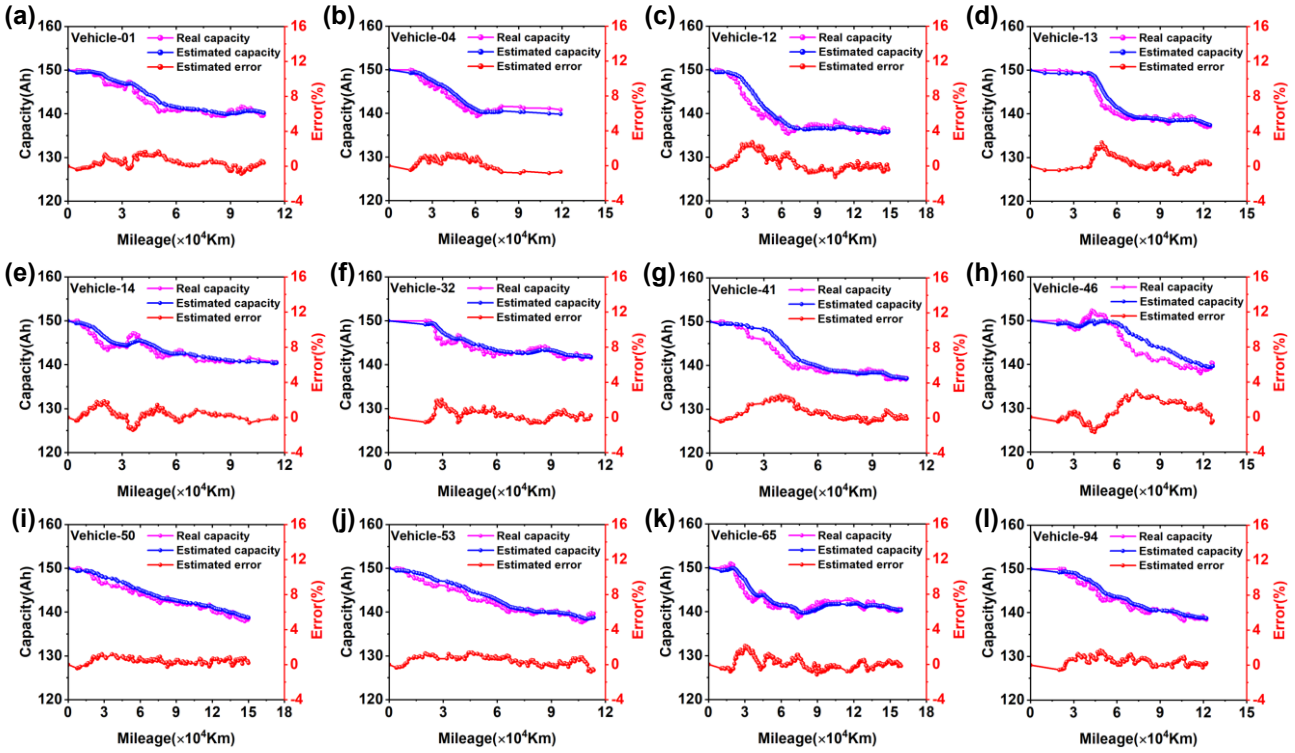


Figure 9. Estimation results of battery capacity for Vehicle-A. (a) Vehicle-01; (b) Vehicle-04; (c) Vehicle-12; (d) Vehicle-13; (e) Vehicle-14; (f) Vehicle-32; (g) Vehicle-41; (h) Vehicle-46; (i) Vehicle-50; (j) Vehicle-53; (k) Vehicle-65; (l) Vehicle-94.

Figure 10 shows the battery capacity estimation results for Vehicle-B. Compared to the cumulative mileage of Vehicle-A at 10 × 10^4 Km~18 × 10^4 Km, the cumulative mileage of Vehicle-B is at an intermediate level, mainly distributed at 10 × 10^4 Km~15 × 10^4 Km. From Figure 10, it can be seen that although the cumulative mileage of vehicles is generally smaller than that of Vehicle-A, there are still some vehicles whose battery capacity shows significant nonlinear decay (see Vehicle-09, Vehicle-18, and Vehicle-92). Due to the severe nonlinear decay phenomenon in the capacity of Vehicle-92, its capacity estimation error is the largest, at 2.960%, while Vehicle-22 has the highest capacity estimation accuracy due to its small capacity decay, with a maximum estimation error of only −0.28%. Although some vehicles have experienced significant capacity decay, the fusion model's estimation results for the vast majority of vehicles are consistent with the decay trend of KF filtering results, indicating that the fusion model has strong stability.

Figure 11 shows the capacity estimation result of Vehicle-C. Compared to Vehicles A and B, Vehicle-C has the shortest driving range, mainly distributed between 2 × 10^4 Km~6 × 10^4 Km. Therefore, there is no serious nonlinear attenuation phenomenon. Moreover, due to the relatively short driving range of the relevant vehicles, only a small amount of charging data is included in the capacity estimation based on the screening criteria of charging ΔSOC greater than 70%. Therefore, the capacity estimation results of the proposed fusion model are basically consistent with the attenuation trend of the capacity labels, and the accuracy of capacity estimation is significantly higher than that of Vehicle-A and Vehicle-B. The capacity estimation error of Vehicle-58 is the largest, only 1.942%, which is much smaller than that of Vehicles-A and B.

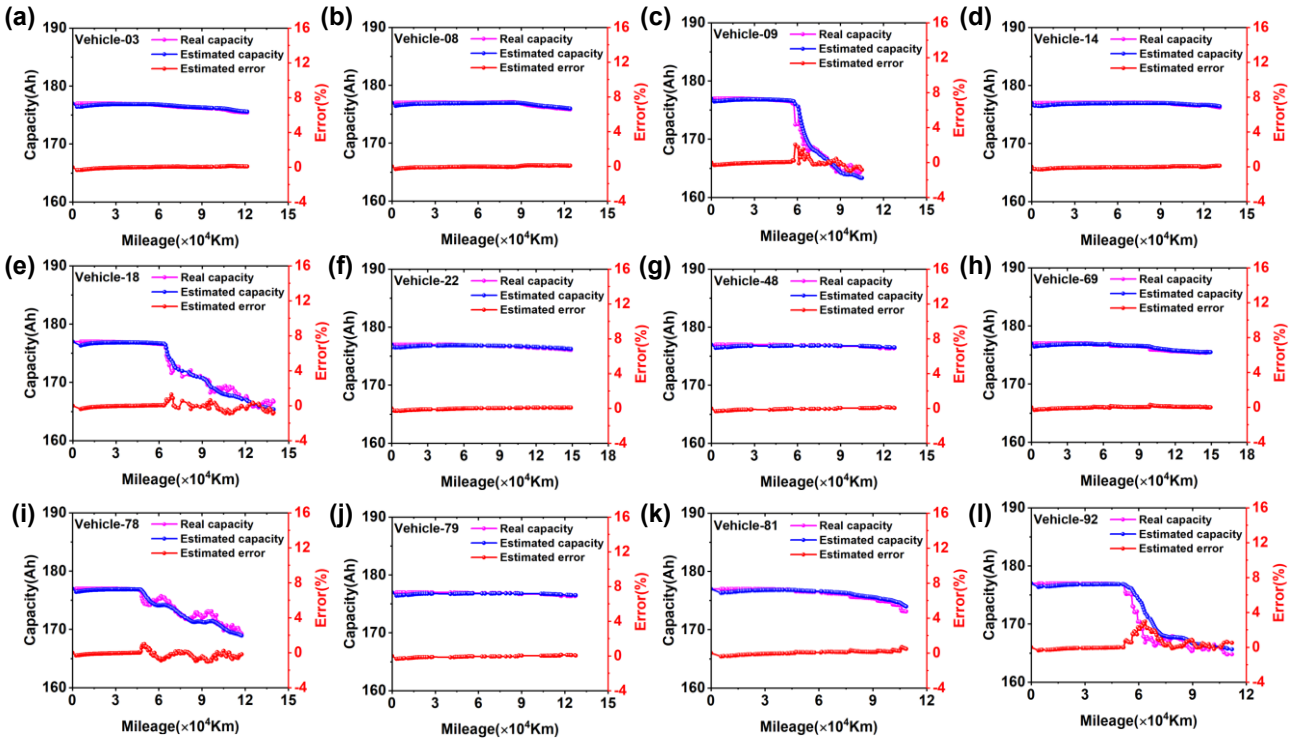


Figure 10. Estimation results of battery capacity for Vehicle-B. (a) Vehicle-03; (b) Vehicle-08; (c) Vehicle-09; (d) Vehicle-14; (e) Vehicle-18; (f) Vehicle-22; (g) Vehicle-48; (h) Vehicle-69; (i) Vehicle-78; (j) Vehicle-79; (k) Vehicle-81; (l) Vehicle-92.

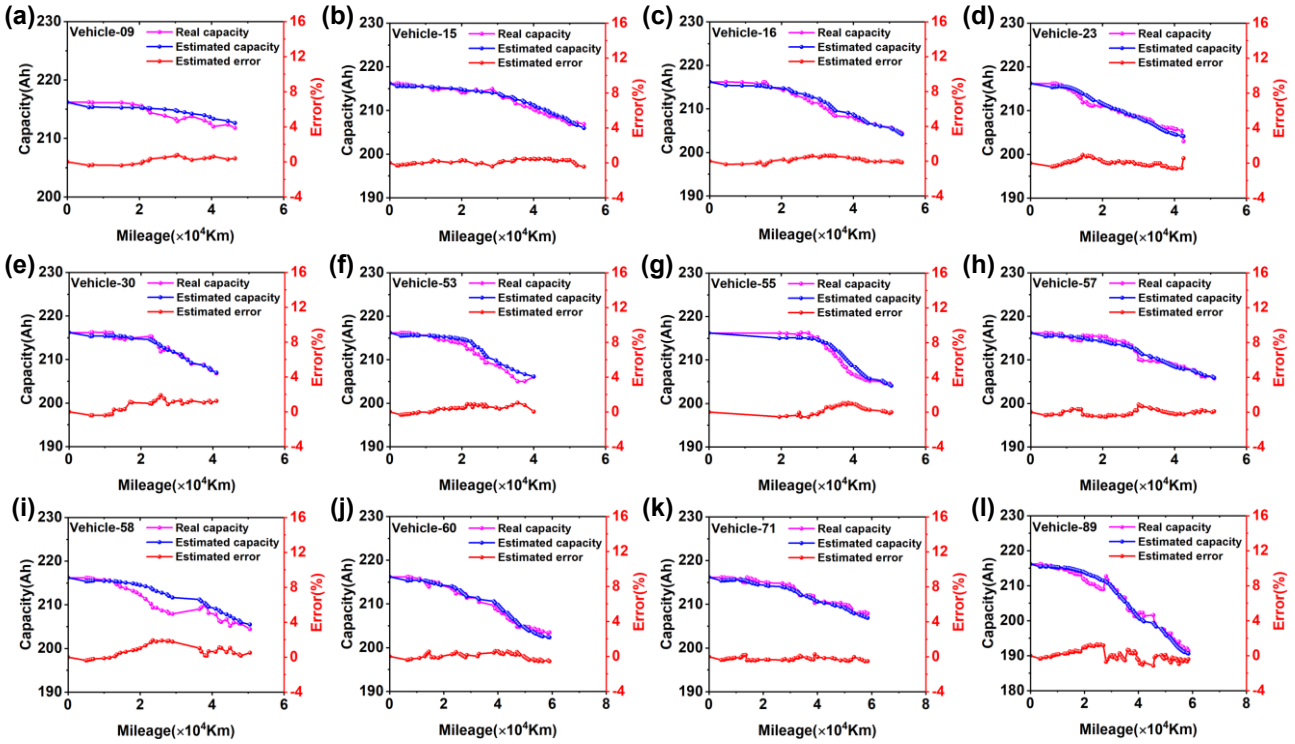


Figure 11. Estimation results of battery capacity for Vehicle-C. (a) Vehicle-09; (b) Vehicle-15; (c) Vehicle-16; (d) Vehicle-23; (e) Vehicle-30; (f) Vehicle-53; (g) Vehicle-55; (h) Vehicle-57; (i) Vehicle-58; (j) Vehicle-60; (k) Vehicle-71; (l) Vehicle-89.

The SOH of a battery is an important indicator reflecting its lifespan decay, so here we further calculate its SOH based on the capacity estimation results of each battery.

Based on the capacity estimation results in Figures 9–11, this study further estimated the SOH values of each vehicle, as shown in Figure 12. The R^2 values of Vehicles-A/B/C are 0.966, 0.983, and 0.981, respectively. From the R^2 values, it can be seen that the SOH estimation results of Vehicles-B and C are better than those of Vehicle-A. Moreover, it can be observed in Figure 12c that although the cumulative driving range of Vehicle-C is generally short, there are still some vehicles with SOH below 90%, which may be due to severe calendar decay of the corresponding vehicles. Furthermore, based on the SOH estimation results, we calculated the maximum error MAE, MAPE, and RMSE. The results are shown in Table 6. From the results in the table, it can be seen that the SOH estimation of vehicle C is the best, which is consistent with our previous capacity estimation analysis results. The maximum errors of SOH for Vehicle-A/B/C are 2.974%, 2.960%, and 1.942%, respectively. Vehicle-B has the highest MAE, MAPE, and RMSE values.

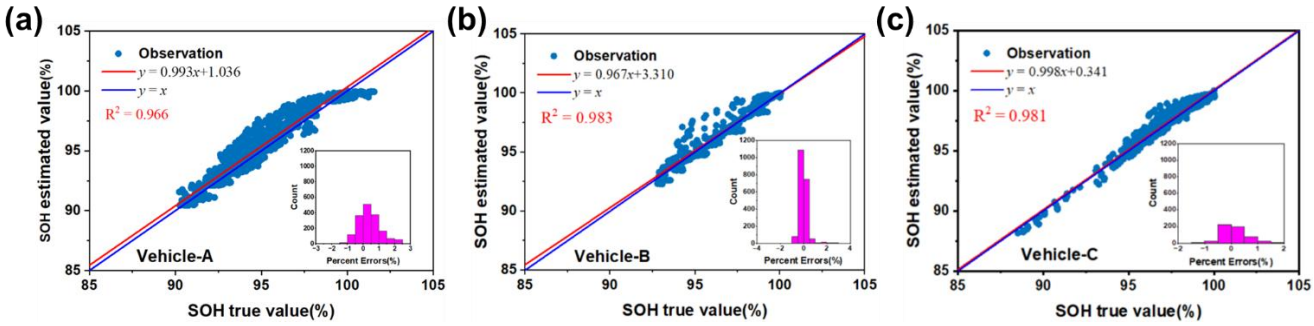


Figure 12. SOH estimation error of fusion model. (**a**) SOH estimation error of Vehicle-A; (**b**) SOH estimation error of Vehicle-B; (**c**) SOH estimation error of Vehicle-C.

Table 6. Comparison of model performance under different vehicle brands.

Vehicle Brands	*Max Error* (%)	*MAE* (%)	*MAPE* (%)	*RMSE* (%)	R^2
Vehicle-A	2.974	0.328	0.341	0.433	0.966
Vehicle-B	2.960	0.681	0.693	0.846	0.983
Vehicle-C	1.942	0.101	0.102	0.164	0.981

5. Conclusions

In response to the limitations of data-driven models and empirical models, this study proposes a DEKF fusion estimation method that combines the advantages of both. The dynamic updating of Arrhenius empirical decay model parameters and the fusion estimation of capacity results were achieved through two independent EKFs, effectively improving the accuracy and robustness of predictions. This method not only fully utilizes the real-time nature of real vehicle data but also optimizes model parameters through historical data, significantly improving the adaptability of the model.

(1) This study proposed a method for obtaining battery capacity labels based on SOC correction and KF for real vehicle charging data; the battery capacity label obtained by this method can accurately describe the trend of battery capacity degradation in real vehicle environments.

(2) The proposed capacity fusion estimation method was validated using data from 36 actual vehicles of three vehicle brands. The maximum estimation error of capacity under a driving range of 2×10^4 Km~18×10^4 Km was 2.974%, which can meet the demand for capacity estimation in actual vehicle environments.

(3) Based on the battery capacity estimation results, accurate estimation of the SOH of the battery under actual vehicle operating conditions has been achieved. The R^2 values for SOH estimation of Vehicles-A/B/C are 0.966, 0.983, and 0.981, respectively.

Author Contributions: Conceptualization, D.Q. and X.L.; methodology, D.Q.; software, Z.C.Z.; validation, X.S., Z.C.Z. and X.L.; formal analysis, D.Q.; investigation, Z.C.Z.; resources, X.J.L.; data curation, Z.W.Z.; writing—original draft preparation, D.Q.; writing—review and editing, X.L.; visualization, D.Q.; supervision, X.L.; project administration, D.Q., and X.L.; funding acquisition, X.L.

Funding: This research is supported by National Natural Science Foundation of China (No. 52507261, 52577238) and Shanghai Sailing Program (24YF2730300).

Data Availability Statement: The data presented in this study are available on request from the corresponding author. The data are not publicly available due to [privacy/commercial] restrictions.

Conflicts of Interest: The authors declare that they have no known competing financial interests or personal relationships that could have appeared to influence the work reported in this paper.

References

1. Sulzer, V.; Mohtat, P.; Aitio, A.; Lee, S.; Yeh, Y.T.; Steinbacher, F.; Khan, M.U.; Lee, J.W.; Siegel, J.B.; Stefanopoulou, A.G.; et al. The challenge and opportunity of battery lifetime prediction from field data. *Joule* **2021**, *5*, 1934–1955. https://doi.org/10.1016/j.joule.2021.06.005.
2. Rogelj, J.; Huppmann, D.; Krey, V.; Riahi, K.; Clarke, L.; Gidden, M.; Nicholls, Z.; Meinshausen, M. A new scenario logic for the Paris Agreement long-term temperature goal. *Nature* **2019**, *573*, 357–363. https://doi.org/10.1038/s41586-019-1541-4.
3. Su, C.; Yuan, X.; Tao, R.; Umar, M. Can new energy vehicles help to achieve carbon neutrality targets? *J. Environ. Manag.* **2021**, *297*, 113348. https://doi.org/10.1016/j.jenvman.2021.113348.
4. Liu, Z.; Deng, Z.; He, G.; Wang, H.; Zhang, X.; Lin, J.; Qi, Y.; Liang, X. Challenges and opportunities for carbon neutrality in China. *Nat. Rev. Earth Environ.* **2021**, *3*, 141–155. https://doi.org/10.1038/s43017-021-00244-x.
5. Armand, M.; Tarascon, J.M. Building better batteries. *Nature* **2008**, *451*, 652–657. https://doi.org/10.1038/451652a.
6. Han, J.; Khalatbarisoltani, A.; Yang, Y.; Hu, X. Energy Management in Plug-In Hybrid Electric Vehicles: Preheating the Battery Packs in Low-Temperature Driving Scenarios. *IEEE Trans. Intell. Transp. Syst.* **2024**, *25*, 1978–1991. https://doi.org/10.1109/TITS.2023.3317637.
7. Wei, X.; Liu, F.; Liu, Z.; Cheng, X.; Zhu, W.; Xie, C. Degradation mechanisms of lithium-ion power batteries under rapid temperature variations in low-temperature environments. *J. Power Sources* **2025**, *656*, 238070. https://doi.org/10.1016/j.jpowsour.2025.238070.
8. Attia, P.M.; Grover, A.; Jin, N.; Severson, K.A.; Markov, T.M.; Liao, Y.-H.; Chen, M.H.; Cheong, B.; Perkins, N.; Yang, Z.; et al. Closed-loop optimization of fast-charging protocols for batteries with machine learning. *Nature* **2020**, *578*, 397–402. https://doi.org/10.1038/s41586-020-1994-5.
9. Wei, M.; Ye, M.; Zhang, J.; Ma, Y.; Li, Y.; Xu, C.; Zhang, C.; Zhang, G. Mechanistic-probabilistic learning fusion approach for state of health estimation in $LiFePO_4$ batteries under high-rate discharge cycling. *Energy* **2025**, *333*, 137281. https://doi.org/10.1016/j.energy.2025.137281.
10. Li, Y.; Qu, X.; Huang, J.; Fu, G.; Chen, X.; Li, K.; Shen, W.; Lin, Y. Insights into the stress-induced acceleration mechanism on calendar aging of lithium-ion battery. *J. Power Sources* **2025**, *648*, 237415. https://doi.org/10.1016/j.jpowsour.2025.237415.
11. Lam, V.N.; Cui, X.; Stroebl, F.; Uppaluri, M.; Onori, S.; Chueh, W.C. A decade of insights: Delving into calendar aging trends and implications. *Joule* **2025**, *9*, 101796. https://doi.org/10.1016/j.joule.2024.11.013.
12. Zhu, J.; Darma, M.S.D.; Knapp, M.; Sorensen, D.R.; Heere, M.; Fang, Q.; Wang, X.; Dai, H.; Mereacre, L.; Senyshyn, A.; et al. Investigation of lithium-ion battery degradation mechanisms by combining differential voltage analysis and alternating current impedance. *J. Power Sources* **2020**, *448*, 227575. https://doi.org/10.1016/j.jpowsour.2019.227575.
13. Kang, C.; Liu, W.-W.; Zhao, W.; Lv, B.; Ding, W.-W. In situ transition metal oxide doping for simultaneous conductivity enhancement and structural stabilization of silicon-carbon anodes. *J. Energy Storage* **2026**, *141*, 119366. https://doi.org/10.1016/j.est.2025.119366.
14. Zhang, G.; Wei, X.; Han, G.; Dai, H.; Zhu, J.; Wang, X.; Tang, X.; Ye, J. Lithium plating on the anode for lithium-ion batteries during long-term low temperature cycling. *J. Power Sources* **2021**, *484*, 229312. https://doi.org/10.1016/j.jpowsour.2020.229312.
15. Chen, Z.; Zhang, C.; Cai, X.; Liu, M.; Qiao, B.; Zhang, L.; Jiang, J.; Yang, X.-G. Operando detection for lithium plating in lithium-ion batteries via expansion force signal decoupling. *J. Power Sources* **2026**, *661*, 238644. https://doi.org/10.1016/j.jpowsour.2025.238644.
16. Xu, H.; Li, S.; Zhang, C.; Chen, X.; Liu, W.; Zheng, Y.; Xie, Y.; Huang, Y.; Li, J. Roll-to-roll prelithiation of Sn foil anode suppresses gassing and enables stable full-cell cycling of lithium ion batteries. *Energy Environ. Sci.* **2019**, *12*, 2991–3000. https://doi.org/10.1039/c9ee01404g.
17. Heiskanen, S.K.; Kim, J.; Lucht, B.L. Generation and Evolution of the Solid Electrolyte Interphase of Lithium-Ion Batteries. *Joule* **2019**, *3*, 2322–2333. https://doi.org/10.1016/j.joule.2019.08.018.

18. Gervillie-Mouravieff, C.; Bao, W.; Steingart, D.A.; Meng, Y.S. Non-destructive characterization techniques for battery performance and life-cycle assessment. *Nat. Rev. Electr. Eng.* **2024**, *1*, 547–558. https://doi.org/10.1038/s44287-024-00069-y.
19. Zhu, J.; Xu, W.; Knapp, M.; Darma, M.S.D.; Mereacre, L.; Su, P.; Hua, W.; Liu-Theato, X.; Dai, H.; Wei, X.; et al. A method to prolong lithium-ion battery life during the full life cycle. *Cell Rep. Phys. Sci.* **2023**, *4*, 101464. https://doi.org/10.1016/j.xcrp.2023.101464.
20. Chen, Z.; Wang, K.; Jiao, M.; Xiong, R. Synergistic internal temperature estimation and fault diagnosis of lithium-ion batteries via online sequential extreme learning machine. *J. Energy Storage* **2025**, *139*, 118750. https://doi.org/10.1016/j.est.2025.118750.
21. Lyu, Z.; Jin, Z.; Li, X.; Wang, H.; Wu, L.; Chen, Y. From tradition to innovation: Evolution and trade-offs of lithium-ion battery state of health estimation methods. *J. Energy Storage* **2026**, *144*, 119730. https://doi.org/10.1016/j.est.2025.119730.
22. Shu, X.; Shen, J.; Guo, F.; Liu, Y.; Zhang, Y.; Chen, Z.; Zhao, H. Towards real-world battery health intelligence: A review of machine learning advances and challenges in SOH estimation. *Etransportation* **2025**, *26*, 100509. https://doi.org/10.1016/j.etran.2025.100509.
23. Wang, T.; Zhu, Y.; Zhang, Z.; Bi, F.; Sun, L.; Kim, T.; Shang, Y. An SOH Estimation Method Within Microvoltage Interval Based on ICA Peak Distribution for Lithium-Ion Batteries. *IEEE Trans. Transp. Electrif.* **2025**, *11*, 9224–9233. https://doi.org/10.1109/TTE.2025.3556447.
24. Sun, J.; Liu, X.; Li, X.; Chen, S.; Xing, S.; Guo, Y. State of health estimation of lithium-ion battery based on constant current charging time feature extraction and internal resistance compensation. *Energy* **2025**, *315*, 134472. https://doi.org/10.1016/j.energy.2025.134472.
25. Li, X.; Yuan, C.; Li, X.; Wang, Z. State of health estimation for Li-Ion battery using incremental capacity analysis and Gaussian process regression. *Energy* **2020**, *190*, 116467. https://doi.org/10.1016/j.energy.2019.116467.
26. Zou, W.; Hu, Z.; Yu, K.; Zhang, H.; Lu, H.; Mao, L. State of health estimation for lithium-ion batteries based on recurrence plot analysis using charging voltage curves. *J. Energy Storage* **2025**, *123*, 116804. https://doi.org/10.1016/j.est.2025.116804.
27. Wu, B.; Yufit, V.; Merla, Y.; Martinez-Botas, R.F.; Brandon, N.P.; Offer, G.J. Differential thermal voltammetry for tracking of degradation in lithium-ion batteries. *J. Power Sources* **2015**, *273*, 495–501. https://doi.org/10.1016/j.jpowsour.2014.09.127.
28. Jiang, B.; Zhu, J.; Wang, X.; Wei, X.; Shang, W.; Dai, H. A comparative study of different features extracted from electrochemical impedance spectroscopy in state of health estimation for lithium-ion batteries. *Appl. Energy* **2022**, *322*, 119502. https://doi.org/10.1016/j.apenergy.2022.119502.
29. Lin, M.Q.; Hu, D.C.; Meng, J.H.; Wu, J. Transfer Learning-Based Lithium-Ion Battery State of Health Estimation With Electrochemical Impedance Spectroscopy. *IEEE Trans. Transp. Electrif.* **2025**, *11*, 7910–7920. https://doi.org/10.1109/TTE.2025.3533540.
30. Wu, M.; Wang, L.; Wu, J. State of health estimation of the $LiFePO_4$ power battery based on the forgetting factor recursive Total Least Squares and the temperature correction. *Energy* **2023**, *282*, 128437. https://doi.org/10.1016/j.energy.2023.128437.
31. Liu, Y.; Lei, A.; Yu, C.; Huang, T.; Yu, Y. An Improved Collaborative Estimation Method for Determining The SOC and SOH of Lithium-Ion Power Batteries for Electric Vehicles. *Energies* **2024**, *17*, 3287. https://doi.org/10.3390/en17133287.
32. Li, Y.; Wang, H.; Wang, C.; Wang, L.; Liao, C.; Wang, L. Unified physics-informed subspace identification and transformer learning for lithium-ion battery state-of-health estimation. *J. Energy Chem.* **2026**, *112*, 350–369. https://doi.org/10.1016/j.jechem.2025.08.060.
33. Yu, Z.; Tian, Y.; Li, B. A simulation study of Li-ion batteries based on a modified P2D model. *J. Power Sources* **2024**, *618*, 234376. https://doi.org/10.1016/j.jpowsour.2024.234376.
34. Fan, W.; Jiang, B.; Wang, X.; Zhu, J.; Liu, H.; Yuan, Y.; Wei, X.; Dai, H. Generalized capacity estimation for retired lithium-ion batteries: Unsupervised electrochemical impedance spectroscopy dimensionality reduction under random retirement conditions. *Energy Storage Mater.* **2026**, *84*, 104836.
35. Ding, S.; Jiang, B.; Liang, Y.; Fu, L.; Qu, C.; Wei, X.; Xie, H.; Dai, H. Decoding Silicon-Driven Degradation: An Adaptive Fusion Framework for Robust Battery Electrode-level Diagnostics. *Energy Storage Mater.* **2026**, *84*, 104874.
36. Cai, L.; Ru, R.; Jin, H.; Meng, J.; Wang, B.; Su, H.; Peng, J.; Cheng, G. An automated method for neural architecture design in lithium-ion battery state of health estimation. *J. Energy Storage* **2025**, *138*, 118636. https://doi.org/10.1016/j.est.2025.118636.
37. Zhang, K.; Jiao, Z.P.; Ma, J.; Zhao, X.; Wang, S.; Yu, M.; Li, S. SOH estimation of battery based on the BIGRU-transformer algorithm considering the hierarchical voltage interval characterization of the discharge curve. *J. Energy Storage* **2025**, *132*, 117770. https://doi.org/10.1016/j.est.2025.117770.
38. Qi, Q.G.; Liu, W.X.; Deng, Z.W.; Li, J.W.; Song, Z.Y.; Hu, X.S. Battery pack capacity estimation for electric vehicles based on enhanced machine learning and field data. *J. Energy Chem.* **2024**, *92*, 605–618. https://doi.org/10.1016/j.jechem.2024.01.047.
39. Qiao, D.; Wei, X.; Fan, W.; Jiang, B.; Lai, X.; Zheng, Y.; Tang, X.; Dai, H. Toward safe carbon-neutral transportation: Battery internal short circuit diagnosis based on cloud data for electric vehicles. *Appl. Energy* **2022**, *317*, 119168.
40. Fang, P.; Chen, G.; Li, J.; Zhang, H.; Wang, Y. Lumped semi-empirical model for lithium-ion batteries considering temperature effects. *J. Energy Storage* **2026**, *141*, 119305. https://doi.org/10.1016/j.est.2025.119305.
41. Jiang, B.; Dai, H.; Wei, X.; Xu, T. Joint estimation of lithium-ion battery state of charge and capacity within an adaptive variable multi-timescale framework considering current measurement offset. *Appl. Energy* **2019**, *253*, 113619. https://doi.org/10.1016/j.apenergy.2019.113619.

42. Qiao, D.; Wang, X.; Lai, X.; Zheng, Y.; Wei, X.; Dai, H. Online quantitative diagnosis of internal short circuit for lithium-ion batteries using incremental capacity method. *Energy* **2022**, *243*, 123082.
43. Nyachionjeka, K.; Abd-Elrady, E.; Bayoumi, E.H.E. Physics-Informed Cross-Domain Deep Learning for Laboratory-to-Field Battery Remaining Useful Life Estimation Under Operational Shifts and Target-Label Scarcity. *Batteries* **2026**, *12*, 274. https://doi.org/10.3390/batteries12080274.

Disclaimer/Publisher's Note: The statements, opinions and data contained in all publications are solely those of the individual author(s) and contributor(s) and not of MDPI and/or the editor(s). MDPI and/or the editor(s) disclaim responsibility for any injury to people or property resulting from any ideas, methods, instructions or products referred to in the content.